Electron Energy Loss Spectroscopy Study of the Full Plasmonic Spectrum of Self-Assembled Au−Ag Alloy Nanoparticles: Unraveling Size, Composition, and Substrate Effects

Yueying Wu,[†,#] Guoliang Li,[‡,#] Charles Cherqui,[§] Nicholas W. Bigelow,[§] Niket Thakkar,[‖] David J. Masiello,*[,§,‖] Jon P. Camden,*[,‡] and Philip D. Rack*[,†,⊥]

[†]Department of Materials Science and Engineering, University of Tennessee, Knoxville, Tennessee 37996, United States
[‡]Department of Chemistry and Biochemistry, University of Notre Dame, Notre Dame, Indiana 46556, United States
[§]Department of Chemistry and [‖]Department of Applied Mathematics, University of Washington, Seattle, Washington 98195, United States
[⊥]Center for Nanophase Materials Sciences, Oak Ridge National Laboratory, Oak Ridge, Tennessee 37831, United States

⑤ *Supporting Information*

ABSTRACT: We report the self-assembly of ultrasmooth $Au_xAg_{1−x}$ nanoparticles with homogeneous composition via pulsed laser-induced dewetting (PLiD). The nanoparticles are truncated nanospheres that sustain unique plasmonic features. For the first time an electron energy loss spectroscopy (EELS) study elucidating the size and composition effects on the plasmonic modes of truncated $Au_xAg_{1−x}$ nanospheres is carried out. EELS characterization captures a linear red-shift in both bright and dark modes as a function of the atomic fraction of Au and a progressive red-shift of all modes as the size increases. The results are interpreted in the context of Mie theory and electron beam simulations. Armed with the full plasmonic spectrum of the $Au_xAg_{1−x}$ system, the truncated spheres and their ordered arrays synthesized via PLiD have promise as elements in advanced photonic devices.

KEYWORDS: *plasmonics, alloy nanoparticles, electron energy loss spectroscopy, dewetting, self-assembly*
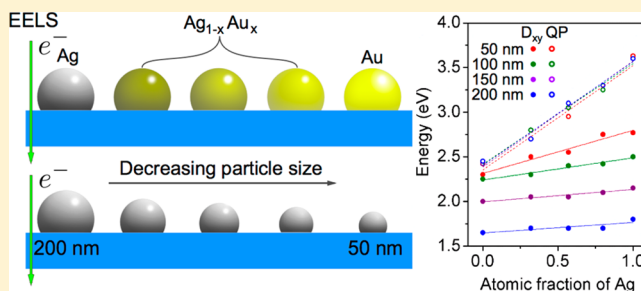
The localized surface plasmon resonances (LSPRs) supported by metallic nanoparticles provide significant enhancement of the electromagnetic field in the vicinity of the nanoparticle surface. This unique property leads to the use of LSPRs in a wide range of applications,[1] such as surface-enhanced Raman spectroscopy,[2,3] sensing,[4,5] imaging,[6] photocatalysis,[7] and photovoltaics.[8,9] Furthermore, the engineering, tuning, and controlling of light below the diffraction limit enable the miniaturization of photonic circuits and the on-chip integration of photonic and electronic systems.[10,11] These functionalities are closely related to the tunability of LSPRs, which have been intensively explored through controlling the shape, size, and dielectric environment of nanoparticles.[12,13] Alloying metallic nanoparticles provides another avenue to manipulate/tune the frequency and lifetime of LSPRs[14−17] and has demonstrated advantages in various applications.[6,17−23] Alloys exhibit not only distinct optical properties when compared to their individual elemental counterparts[14,15,20,23] but also additional functionalities such as enhanced chemical stability of plasmonic materials prone to oxidation (such as Ag, Cu)[17,24] or improved biocompatibility of Ag nanoparticles.[18] The ability to effectively synthesize and engineer alloy nanostructures is therefore an important complement to the often-studied influence of size and geometry.

To realize desirable plasmonic functionalities based on elemental or alloyed plasmonic materials, controlled nanoscale synthesis of metallic nanostructures has been explored extensively in the past decade. To this end, there are essentially two synthesis paradigms: (1) bottom-up self- and directed-assembly and (2) top-down lithographic methods. Of the bottom-up methods, gold and silver nanoparticles of variable composition and geometry such as nanospheres,[13,17] nanorods,[25] core−shell nanoparticles,[26,27] cubes,[28] octahedra,[29] tetrahedra,[30] and icosahedra[31] are commonly synthesized using wet-chemical methods. Single crystals and atomically flat surfaces can be realized via well-controlled chemical synthesis that can reduce greater losses and damping of surface plasmons due to surface roughness or grain boundaries.[28,32−34] However, organizing wet-chemically synthesized nanoparticles into precise, complex, and hierarchical ensembles is challenging.[35,36] Conversely, planar metallic structures and ordered arrays are traditionally constructed via top-down lithography and deposited by physical vapor deposition. These precisely defined geometries and highly ordered elemental/alloy arrays
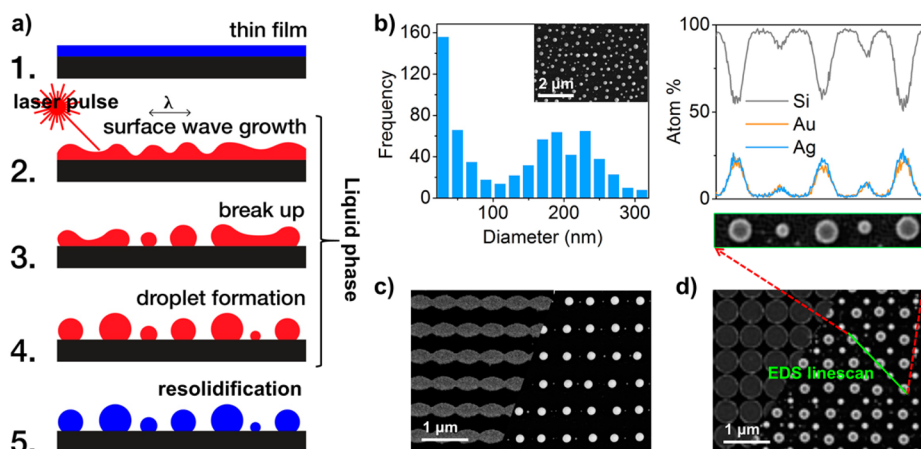
Figure 1. (a) Schematic illustrating the progression in a pulsed laser-induced self-assembly process where an initial thin film is (1) deposited and pulse laser irradiated to form a liquid film in which (2) surface waves grow via liquid/solid interactions and eventually (3 and 4) evolve into assembled nanoparticles and are (5) finally resolidified. (b) Histogram of the resultant nanoparticle size distribution from a 20 nm Ag film (inset is a representative scanning electron microscope image of the nanoparticle distribution). (c) Lithographically patterned silver lines (left) and the resultant ordered 1D silver nanoparticle arrays (right) formed via PLiD. (d) Lithographically patterned $Au_{0.5}Ag_{0.5}$ film (left) and resultant ordered $Au_{0.5}Ag_{0.5}$ 2D nanoparticle array (right) formed via PLiD. (d, top panel) Au, Ag, and Si EDS line scans of the $Au_{0.5}Ag_{0.5}$ nanoparticle array.

generate various coupled plasmonic resonances and novel functionalities compared to randomly distributed nanoparticles.[37−39] Despite the well-defined geometries and sizes produced via traditional lithography, the resulting sharp corners and planar surfaces are usually unstable at elevated temperature, and traditional lift-off methods used in lithography patterning also produce edge roughness.

Recently, pulsed laser-induced dewetting (PLiD) has been explored as a fast and efficient self-assembly technique for generating elemental[40−42] and bimetallic[43−46] nanoparticles. The PLiD technique involves irradiating a thin (typically <50 nm) metal film supported on a substrate with a 10−20 ns laser pulse with sufficient intensity to briefly melt the film. During the liquid lifetime (tens of nanoseconds), liquid phase instabilities[40,41,47] and hydrodynamics dictate the breakup and transport of the liquid film, resulting in arrays of truncated nanospheres whose wetting angle with the underlying substrate is governed by surface energies of the system. Conveniently the resultant solid nanoparticles are remarkably smooth due to their rapid solidification from the liquid phase. Recently,[48] the disperse nanoparticle size distribution that results from the natural 2D film instabilities was exploited to determine the full plasmonic spectrum of truncated silver nanoparticles ranging from 20 to 1000 nm. Importantly, using a confluence of top-down lithography and PLiD-directed assembly, highly ordered one-[40,49] and two-dimensional[44,50] nanoparticle arrays with hierarchical architectures have been realized. Thus, the PLiD technique is a powerful method for direct assembly of both elemental and alloyed functional plasmonic nanostructures and devices.

In the present work we report the experimental and theoretical electron energy loss spectroscopy (EELS) characterization of truncated $Au_xAg_{1−x}$ alloy nanospheres synthesized via the PLiD of Au−Ag thin films. We demonstrate that the $Au_xAg_{1−x}$ alloy nanoparticles formed via PLiD form a solid solution over the range of compositions studied, which is consistent with the equilibrium phase diagram. Furthermore, the nanoparticles that result have not only an ultrasmooth surface but also a uniform alloy composition over each particle. The truncated sphere−substrate system exhibits intriguing

optical properties compared to other geometries and is suitable for multiple applications.[51−53] Similar structures were shown to have a high fraction of light scattered into the substrate[54] and exhibit strong interface localization,[48,51] which suggests the potential of such a geometry in photovoltaics and photocatalytic devices.[48,51,55] It has also been shown that greater sensitivity to polarization and incidence angle can arise from the broken symmetry of a hemispherical nanoparticle on dielectric substrates.[53] Despite the numerous studies of the plasmonic behavior of Au−Ag alloys of various geometries,[17,21,26,56−58] the present work reveals for the first time a complete mapping of the LSPR modes on identically synthesized truncated $Au_xAg_{(1−x)}$ alloy spheres over a large size and composition range. The combination of transmission electron microscopy (TEM) and EELS provides high spatial and energy resolution imaging of both bright and dark plasmonic modes as a function of size and composition that are not fully accessible via optical characterization. The experiments are interpreted in the context of Mie theory and full-wave electrodynamics simulations using the well-documented electron-driven discrete dipole approximation (e-DDA).[59]

■ RESULTS AND DISCUSSION

Nanoparticle Morphology and Structures. Figure 1a schematically illustrates the progression of the PLiD self-assembly process. The initially thin solid film is irradiated with a 10−20 ns pulsed laser sufficient to rapidly melt the film for typical durations on the order of tens of nanoseconds.[44] For a thin liquid metallic film, dewetting is dominated by a confluence of nucleation and spinodal dewetting instabilities. Film rupture via spinodal instabilities occurs by amplification of unstable surface thermal waves selected by the interface potential between the liquid film and substrate.[47] Subsequent to film rupture, the far-from-equilibrium geometry induces hydrodynamic transport dominated by a balance of capillary and viscous forces. Simultaneous to the liquid phase transport, heat is dissipated from the system and the nanoparticles rapidly resolidify with a size and spacing correlated to the fastest growing surface perturbation wavelengths.[47]
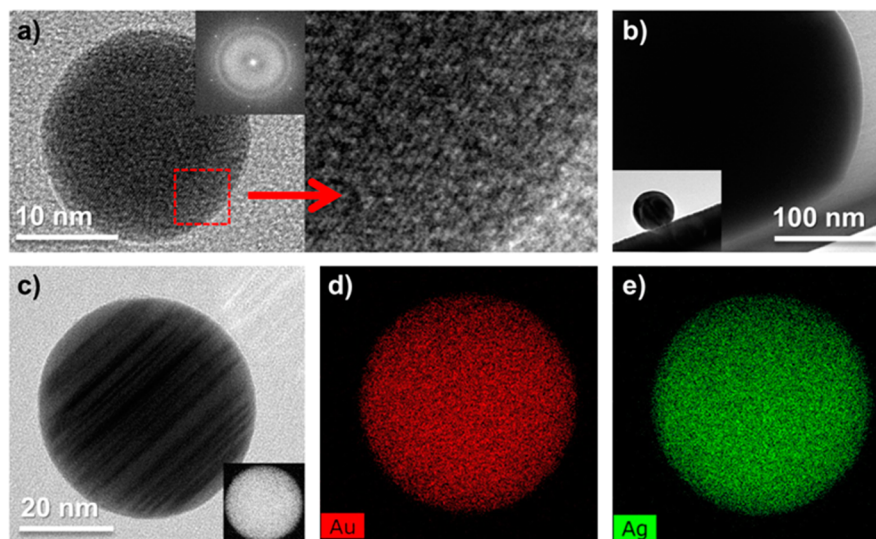
Figure 2. (a and c) HRTEM images of $Au_{0.43}Ag_{0.57}$ alloy nanoparticles of 20 and 46 nm diameter, respectively. (c, inset) HAADF image of the 46 nm diameter $Au_{0.43}Ag_{0.57}$ alloy nanoparticle. (b) TEM side view (90° tilted) images of two $Au_{0.43}Ag_{0.57}$ alloy nanoparticles. (d and e) EDX elemental mapping of Au and Ag in the $Au_{0.43}Ag_{0.57}$ alloy nanoparticle shown in c (46 nm diameter).
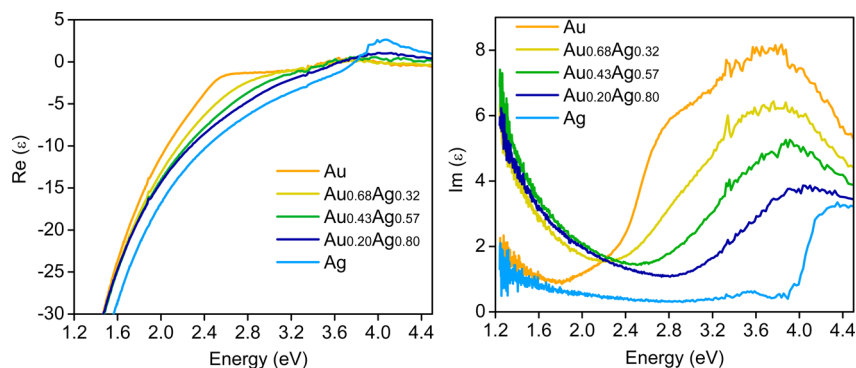

Figure 3. Measured dielectric functions of Au, Ag, and the three alloy films.

The resultant nanoparticle size histogram generated via PLiD from a 20 nm Ag film is illustrated in Figure 1b with an inset of a representative scanning electron microscope image of the nanoparticle array. The estimated average nanoparticle spacing is ~670 nm, which conveniently minimizes interparticle coupling during the EELS characterization. As described earlier, highly ordered 1D or 2D arrays of smooth nanospheres can be realized by lithographic patterning of thin film nanostructures prior to PLiD (directed assembly). Figure 1c displays scanning electron micrographs of the patterned one-dimensional silver lines (left) and the resulting ordered 1D nanoparticle arrays (right). Figure 1d shows scanning electron micrographs of a (left) patterned nanostructure array and the resulting 2D nanoparticle array (right) with ~$Au_{0.5}Ag_{0.5}$ atomic composition. The top panel of Figure 1d is a compilation of Au, Ag, and Si energy dispersive X-ray spectroscopy (EDX) line scans (see inset of higher magnification nanoparticle array image) confirming the ~50/50 atomic as-deposited composition is preserved during the PLiD process.

Next we demonstrate the resultant nanoparticle morphology and crystalline structure of individual $Au_{0.43}Ag_{0.57}$ alloy nanoparticles generated via PLiD of a 2D film. The crystalline structure of the nanoparticles is examined using high-resolution transmission electron microscopy (HRTEM) (examples shown in Figure 2a−c). Most of the nanoparticles are polycrystalline

with an average grain size of a few tens of nanometers. However, single-crystal particles are observed in small nanoparticles (~20 nm) as demonstrated in Figure 2a, indicating the potential to produce low-loss single-crystal nanoparticles at small size scale using this method. As demonstrated in the inset of Figure 2c, the high angle annular dark field (HAADF) image of a 46 nm diameter $Au_{0.43}Ag_{0.57}$ alloy nanoparticle confirms no distinct Au- or Ag-rich domains. Figure 2d and e are the corresponding EDS maps of the elemental distributions of Au and Ag collected on the 46 nm nanoparticle, which further verify the homogeneity of the alloy. It is well known that Au and Ag are completely miscible due to their similar lattice constant (4.08 Å for Au and 4.09 Å for Ag) and crystal structure (face-centered cubic). In addition to the homogeneity, Figure 2 illustrates that the resultant truncated spheres are ultrasmooth due to the rapid solidification from the liquid phase. The spherical shape results from the liquid phase minimum energy, which is isotropic and does not have any crystallographic bias. The homogeneity is further demonstrated in the EELS characterization.

An important geometric factor of the truncated nanospheres is the resultant contact angle that the Au, Ag, and alloy particles make with the silicon nitride substrates. Figure 2b illustrates a tilted TEM image revealing a contact angle of ~135° governed by the well-known Young's equation $\gamma_{LV} \cos \theta = \gamma_{SV} - \gamma_{SL}$,
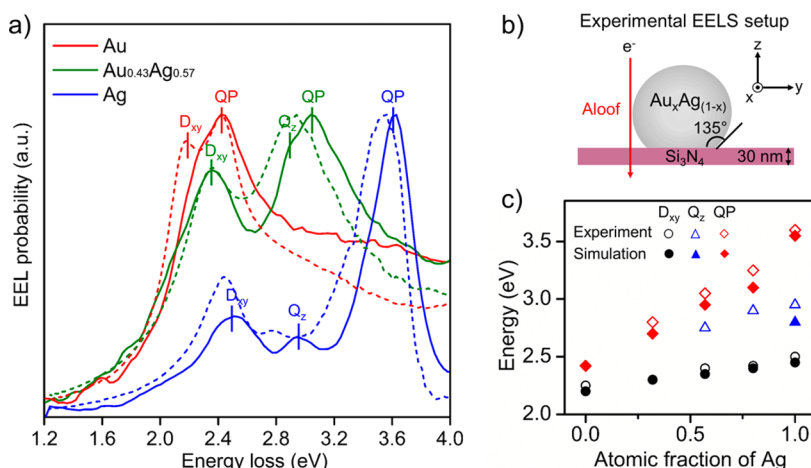
Figure 4. (a) Aloof EEL spectra (experiment, solid; simulation, dashed) for 100 nm diameter particles. The peaks for the D_{xy}, Q_z, and QP for the EELS measurements are labeled in the graph. (b) Illustration of beam setup. (c) Dependence of LSPR mode energy on alloy composition.

where γ_{LV}, γ_{SV}, and γ_{SL} are the liquid−vapor, solid−vapor, and solid−liquid interfacial energy, respectively. Although a slight difference in contact angle between the two metals is expected due to the slight interfacial energy differences, a consistent contact angle of ∼135 ± 5° is observed over the entire composition range. Importantly, the films were synthesized with no adhesion layer such as Ti or Cr, so the results are not convoluted with impurities.

Dielectric Constants of $Au_xAg_{1−x}$ Alloy Films. Many studies have shown that the often-used composition-weighted average of the dielectric functions (ε) of the pure metals fails to predict those of the alloys,[14,16] as it is not able to reproduce both a quasi-linear shift of the interband transition thresholds in alloys observed experimentally and also the changes in the free electron behavior that results in additional plasmonic damping upon alloying. While several experimental Au−Ag alloy dielectric function measurements are available in the literature,[15,16,60] it is well known that ε is sensitive to the synthesis process. Therefore, an accurate measurement of ε is important for simulations to precisely determine the plasmonic behavior of alloys. For this purpose, the dielectric functions of both pure Au and Ag and several alloy compositions are determined from a fit of measured ellipsometric spectra of the sputter-deposited films as described in the Supporting Information (with a table of the values listed).

The measured dielectric functions are shown in Figure 3. The measured imaginary part of ε shows that the interband transition threshold progressively shifts from ∼2.4 eV (for Au) to ∼4 eV (for Ag), which agrees well with the trend pointed out by Gaudry.[57] Meanwhile, the alloys exhibit higher absorption compared to the pure metals in the low-energy region.[57] The experimentally determined dielectric functions are used in the presented e-DDA simulations. We point out that, without using any fitting parameters, excellent agreement between experiment and theory is obtained for the whole size and composition range considered in this study. The successful prediction of alloyed nanoparticle properties using the experimentally determined bulk dielectric functions is not surprising considering that the size range studied is not in a regime where electron-surface scattering or electron spill-out effects dominate the physics.

Examination of LSPR Modes Using EELS. The LSPR modes of a substrate-supported truncated sphere are similar to

those of a sphere in free space when the contact angle between the particle and the substrate is high and/or the particle is large. However, when the particle or the contact angle with the substrate is small, the specific structural features of truncated spheres cannot be ignored. To describe these modes over the size distribution considered here, we take the well-known Mie modes of the sphere as a starting point. Truncating the sphere gives the system edges and faces, which generate a new set of LSPR modes that concentrate surface charge at these geometric features. The presence of the substrate enables otherwise orthonormal LSPR modes to interact. This interaction mediates substrate-induced LSPR mode-mixing and LSPR localization toward the substrate or away from it, depending on the mode in question. Since energy must go into polarizing the substrate, its presence lowers the overall energy of the system, leading to a red-shift in the spectrum. Collectively, these effects conspire to give the substrate-dressed LSPR modes of a truncated nanosphere some interesting features, such as a far-field optically accessible interface localization, which could prove useful in solar energy harvesting applications.[48] A thorough examination of the LSPR modes of truncated Ag nanospheres synthesized via PLiD was recently reported,[48] and we use the analysis provided there to interpret the EEL spectra of the $Au_xAg_{(1−x)}$ alloy nanoparticles presented here. Additional simulations that explore the role of contact angle on the optical properties of truncated spheres are included in Supporting Information Figure S2.

We first focus on the EELS spectra of Au, Ag, and $Au_{0.43}Ag_{0.57}$ alloy nanoparticles with ∼100 nm diameter (solid lines Figure 4a), as they exhibit the main spectral features found in particles of other sizes. Notably, EELS captures both the bright and dark modes that are not accessible in optical measurements. A complete set of simulated and experimental EELS spectra for particles of five different material compositions spanning ∼20−200 nm in diameter is provided in the Supporting Information. Figure 4a shows the measured and simulated EEL spectra for an aloof beam position. The dashed lines are e-DDA simulations carried out at the same beam position using the measured dielectric functions shown in Figure 3. The three most prominent LSPR modes in Ag truncated nanospheres are[48] two degenerate dipole modes oriented parallel to the substrate with an energy of 2.6 eV,

denoted as D_{xy}, the z-oriented quadrupole mode Q_z, located at 2.8 eV, and the quasiplanar mode QP, located at 3.6 eV.

The spectrum for Au nanoparticles in Figure 4a has the same qualitative features as the spectrum of Ag nanoparticles, but due to the differing dielectric properties of Au and Ag, the D_{xy} and QP LSPR modes are lower in energy. Moreover, the relatively large electron scattering rate in Au causes line width broadening, indicating shorter plasmon lifetimes for systems containing Au. For pure Au, the D_{xy} mode is at 2.3 eV and the QP mode is at 2.4 eV.

The QP mode is a superposition of high-order plasmon modes that is nearly degenerate with the standing wave surface plasmon polariton (SPP) of a metal slab. The maximum order mode supported by the nanoparticle increases with size, resulting in higher order contributions to the EEL spectrum. When this effect is combined with the red-shifting and spreading out of modes with increasing particle size, the spectra appear to exhibit a single peak that is invariant to system parameters. This creates the illusion that the QP mode does not change its energy with particle size or the presence of a substrate. All LSPR modes that the nanoparticle is capable of supporting are bounded above by the SPP frequency because the plane geometry is indistinguishable from an infinite radius sphere, providing an upper bound on the value of the LSP mode energy. Physically, this occurs on particles that are several hundreds of nanometers in size. This is most explicitly seen in the $l \rightarrow \infty$ limit of the LSPR mode energies of a nanosphere (Mie modes) $\hbar\omega_M = \hbar\omega_p[l/(l(\epsilon_\infty + 1) + 1)]^{1/2}$, showing that the system is bounded above by the SPP energy $\hbar\omega_{SPP} = \hbar\omega_p/(\epsilon_\infty + 1)^{1/2}$. The location of the QP mode is thus determined by ϵ_∞, the dielectric contribution due to the metal's core electrons and the plasma frequency ω_p. Figure 5 shows the $l =$
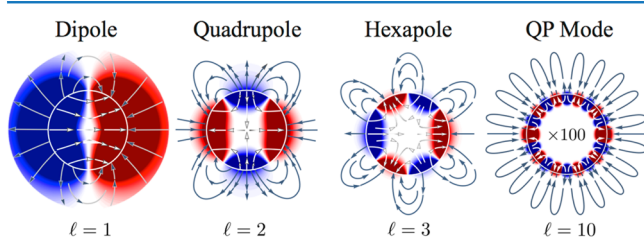

Figure 5. Electric potentials and electric field lines for the LSPR modes of a 20 nm Ag nanosphere for $l = 1$, 2, 3, and 10. As the mode number increases, the LSPR becomes increasingly localized to the nanoparticle surface. The field of the $l = 10$ mode has been multiplied by a factor of 10^2 to make it easier to visualize. The $l = 10$ mode has an energy of $E_{QP} = 3.69$ eV and is representative of the QP mode. However, since the maximal allowed mode is determined by particle size, the QP mode simply refers to the highest order mode supported by the system.

1, 2, 3, and 10 modes of a metallic nanosphere, with the $l = 1$ being the dipole mode and $l = 2$ being the quadrupole mode. At $l = 10$, there is an increased concentration of the electric field to the surface and the LSPR mode is no longer able to resolve the geometry of the nanoparticle, giving rise to the QP mode.

The spectrum for $Au_{0.43}Ag_{0.57}$ in Figure 4a has three distinguishable peaks at 2.4, 2.75, and 3.05 eV. We classify these as the system's D_{xy}, Q_z, and QP modes, respectively. The $Au_{0.43}Ag_{0.57}$ spectrum reveals that while the QP mode is not sensitive to particle size or shape, it is sensitive to the composition of the alloy, indicating that alloys can be used to tailor the properties of LSPRs. The high energy-density of the

QP mode and its sensitivity to the dielectric properties of the metal may be suitable for applications such as plasmonic heating, photocatalysis, and sensing applications.[1−9]

Analyzing $Au_{0.32}Ag_{0.68}$ and $Au_{0.2}Ag_{0.8}$ nanoparticles of the same size provides the LSPR mode energies as a function of alloy composition (Figure 4c). We observe a linear red-shift of the dipole mode (D_{xy}), in agreement with previous work.[14−16] This further confirms that the full alloying of $Au_xAg_{1−x}$ nanoparticles is realized using the PLiD-synthesized nanoparticles. The Q_z mode shows a progressive red-shift as the Au concentration increases; however, it is only weakly excited when the Au concentration is greater than ~43%. For the purposes of simulation, each particle is modeled as a perfectly smooth truncated sphere with spatially uniform composition supported from below by a silicon nitride substrate. As demonstrated in Figure 4 (and Supporting Information Figure S1), the e-DDA simulation results are in excellent agreement with experiments.

The spectral evolution the LSPR modes as a function of inverse particle diameter for particles spanning 20−230 nm in diameter and five alloy compositions are shown in Figure 6a−e. These data are presented as a function of inverse particle diameter to stress the relationship between the LSPR modes of nanoparticles with the SPP modes of a plane.[61] For particles larger than ~250 nm, only the QP mode is observable due to the spatially localized nature of the STEM electron's evanescent electric field compared to the relatively large size of the nanoparticle, which leads to the preferential excitation of high-order modes.[48,62] Simulations are performed for particles 20, 50, 100, 150, and 200 nm in diameter. The results for each mode are included as solid markers with the same color and shape as the experimental results. Both the D_{xy} and Q_z modes show the usual red-shift in mode energy as the particle diameter increases, with the QP mode appearing to be constant with varying particle size. Experimentally measured D_{xy}, Q_z, and QP mode energies are also plotted as a function of particle diameter in Figure 6g, indicating the stronger size dependence of D_{xy} in Ag relative to Au. The size dependence of D_{xy} and Q_z in pure Au and Ag is comparable to previous observations in Au and Ag nanospheres.[63,64]

In general, the overall spectrum red-shifts with increasing Au concentration, suggesting the potential use of alloying to tune LSPR modes to a desired frequency range. To highlight the sensitivity of the LSPR mode energy to alloy composition, we plot the experimentally measured D_{xy} and QP mode energies as a function of the atomic fraction of Ag (Figure 6f) for particle sizes 50, 100, 150, and 200 nm in diameter. A comparison of the slopes of the fitted lines indicates that the D_{xy} mode in small particles is more sensitive to alloy composition than it is in large particles. The plots demonstrate that the QP mode has the highest sensitivity to alloy composition, regardless of particle size. As discussed above, the QP mode can be approximated by the standing wave limit of an SPP ($\hbar\omega_{SPP} = \hbar\omega_p/(\epsilon_\infty + 1)^{1/2}$) and is therefore independent of particle size and is fully determined by the dielectric properties of the alloy. To our knowledge, this is the first known measurement of this effect on the QP mode. The ultrasmooth nature of PLiD-synthesized nanoparticles and the use of measured bulk dielectric data for the nanoparticle alloys allow for excellent agreement between simulation and experiment (Figure 4 and Supporting Information Figure S1). The experimental and simulated EELS spectra for an additional five compositions and five nanoparticle sizes are provided in the Supporting Information.
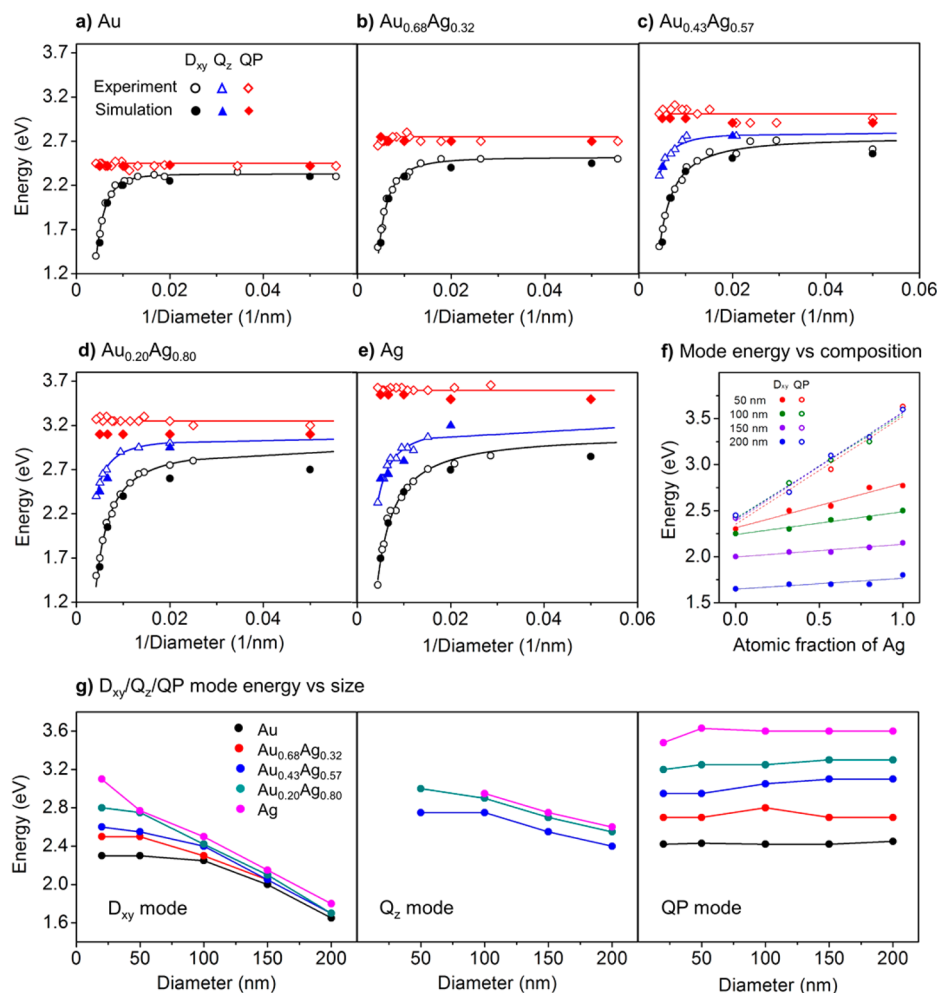
Figure 6. (a−e) Experimental and simulated energy dependence of LSPR modes of a truncated nanosphere as a function of inverse particle diameter. (f) Experimentally measured D_{xy} and QP mode energies as a function of atomic fraction of Ag for five particle sizes. The straight lines are linear fits to the data points. (g) Experimentally measured D_{xy}, Q_z, and QP mode energies as a function of particle diameter.

By using experimentally determined dielectric functions, remarkable agreement between experiment and simulations is obtained across a wide size range in the classical plasmon regime and across the entire Au_xAg_{1-x} composition.

CONCLUSION

In this study, we demonstrate the self-assembly of truncated Au_xAg_{1-x} alloy nanospheres on a supporting substrate via PLiD. The self-assembly process yields ultrasmooth nanoparticle surfaces and uniform alloy compositions over the entire binary Au−Ag composition range. For the first time, the size and composition effects on the substrate-dressed LSPR modes of identically synthesized truncated nanospheres are examined using EELS. The spectra reveal a progressive red-shift of all LSPR modes as a function of size and a linear red-shift of the modes as the atomic fraction of Au is increased. The experimentally measured dielectric functions of the $Au_xAg_{(1-x)}$ alloys enable a precise theoretical analysis of the plasmonic behavior of the alloy nanoparticles. Combined with the ability to direct the assembly of ordered nanoparticle arrays via PLiD, alloyed truncated nanospheres supporting unique and tunable LSPR modes have tremendous promise for advanced optical and photonic circuit applications.

EXPERIMENTAL SECTION

Synthesis of Au, Ag, and $Au_xAg_{(1-x)}$ Alloy Nanoparticles. Au and Ag films and Au−Ag alloy films of ∼20 nm thickness were RF magnetron sputter deposited directly onto 30 nm thick silicon nitride membranes. Three alloy compositions ($Au_{0.2}Ag_{0.8}$, $Au_{0.43}Ag_{0.57}$, and $Au_{0.68}Ag_{0.32}$) were cosputtered using two element targets (Au and Ag). Alloy compositions were controlled by adjusting sputtering rate (RF power) of each target. As the Ag−Au system is a solid solution alloy, we anticipate a homogeneous composition of the cosputtered thin films.[65] The as-deposited films were subsequently irradiated with an 18 ns, 248 nm KrF excimer laser at sufficient fluence (∼40 mJ/cm²) to melt the films. Upon laser melting, liquid phase instabilities and hydrodynamics govern the film breakup and liquid transport, which yields arrays of truncated nanospheres of a size range correlated to the initial film thickness.

Measurement of Dielectric Function for Au, $Au_{0.68}Ag_{0.32}$, $Au_{0.43}Ag_{0.57}$, $Au_{0.2}Ag_{0.8}$, and Ag Films. Optically thick (∼250 nm) Au, Ag, and a continuous combinatorial alloy film ranging from $Au_{0.75}Ag_{0.25}$ to $Au_{0.2}Ag_{0.8}$ were deposited onto silicon nitride coated Si wafers. The dielectric functions for each pure film and eight compositions across the combinatorial sample were measured using a J.A. Woolam M-2000U variable-angle spectroscopic ellipsometer over a wavelength of 245−999 nm. To fit the raw data, the film was represented as a slab of uniform thickness having sharp interfaces and optical properties described by the Cauchy model. The best fit was achieved using a point-by-point regression analysis to minimize the mean squared error. The measured dielectric functions are shown in

EDX Line Scan of $Au_{0.5}Ag_{0.5}$ Ordered Nanoparticle Arrays. An EDX line scan of the $Au_{0.5}Ag_{0.5}$ ordered nanoparticle arrays was performed using a Phenom ProX SEM, at 10 kV acceleration voltage. A ~1.9 μm line consisting of 256 points was scanned through the center of five nanoparticles. The compositions at each point were determined using the PhiZAF correction where the Au M (2.12 keV), Ag L_a (2.984 keV), and Si K_a (1.739 keV) peaks were analyzed. The background subtraction was performed by a simple linear interpolation, and the peaks were fit with Gaussian profiles and corrected for the absorption of the detector window. The result is shown in the top panel of Figure 1d.

EELS Characterization. EELS experiments were performed in a monochromated Carl Zeiss LIBRA 200MC (S) TEM operated at 200 kV. The convergence and collection semiangles used for spectrum acquisition were 9 and 12 mrad, respectively. The energy resolution (full width at half-maximum of the zero-loss peak) is approximately 150 meV. The experimental EEL spectra presented in Figure 4 were obtained by subtracting a normalized background EEL spectrum (taken far away from any particles) from the normalized aloof EEL spectra. The subtraction method is valid because (1) the Si_3N_4 film is uniform in thickness and (2) the inelastic scattering in the aloof position is small enough so as to minimally affect the subsequent substrate signal. No attempt was made to deconvolve the experimental data from the ZLP. Broadening in the numerical simulation may be attributed to the offset between experimentally determined dielectric functions of the thin films and nanoparticles.

■ ASSOCIATED CONTENT

Ⓢ Supporting Information

The Supporting Information is available free of charge on the ACS Publications website at DOI: 10.1021/acsphotonics.5b00548.

    (1) Complete set of experimental and simulated EELS spectra for particles of five different material compositions and five sizes spanning ~20−200 nm in diameter and (2) experimentally determined dielectric functions of Au, Ag, and the three alloy films (PDF)

■ AUTHOR INFORMATION

Corresponding Authors
*E-mail: masiello@chem.washington.edu.
*E-mail: jon.camden@nd.edu.
*E-mail: prack@utk.edu.

Author Contributions
#Y. Wu and G. Li contributed equally to this work.

Notes
The authors declare no competing financial interest.

■ ACKNOWLEDGMENTS

■ REFERENCES

(1) Schuller, J. A.; Barnard, E. S.; Cai, W. S.; Jun, Y. C.; White, J. S.; Brongersma, M. L. Plasmonics for extreme light concentration and manipulation. *Nat. Mater.* **2010**, *9*, 193−204.

(2) Sharma, B.; Frontiera, R. R.; Henry, A. I.; Ringe, E.; Van Duyne, R. P. SERS: Materials, applications, and the future. *Mater. Today* **2012**, *15*, 16−25.

(3) Nie, S. M.; Emery, S. R. Probing single molecules and single nanoparticles by surface-enhanced Raman scattering. *Science* **1997**, *275*, 1102−1106.

(4) Willets, K. A.; Van Duyne, R. P. Localized surface plasmon resonance spectroscopy and sensing. *Annu. Rev. Phys. Chem.* **2007**, *58*, 267−297.

(5) Goken, K. L.; Subramaniam, V.; Gill, R. Enhancing spectral shifts of plasmon-coupled noble metal nanoparticles for sensing applications. *Phys. Chem. Chem. Phys.* **2015**, *17*, 422−427.

(6) Sekhon, J. S.; Malik, H. K.; Verma, S. S. DDA simulations of noble metal and alloy nanocubes for tunable optical properties in biological imaging and sensing. *RSC Adv.* **2013**, *3*, 15427−15434.

(7) Hou, W. B.; Cronin, S. B. A review of surface plasmon resonance-enhanced photocatalysis. *Adv. Funct. Mater.* **2013**, *23*, 1612−1619.

(8) Reineck, P.; Lee, G. P.; Brick, D.; Karg, M.; Mulvaney, P.; Bach, U. A solid-state plasmonic solar cell via metal nanoparticle self-assembly. *Adv. Mater.* **2012**, *24*, 4750−4755.

(9) Chen, H. C.; Chou, S. W.; Tseng, W. H.; Chen, I. W. P.; Liu, C. C.; Liu, C.; Liu, C. L.; Chen, C. H.; Wu, C. I.; Chou, P. T. Large AuAg alloy nanoparticles synthesized in organic media using a one-pot reaction: Their applications for high-performance bulk heterojunction solar cells. *Adv. Funct. Mater.* **2012**, *22*, 3975−3984.

(10) Barnes, W. L.; Dereux, A.; Ebbesen, T. W. Surface plasmon subwavelength optics. *Nature* **2003**, *424*, 824−830.

(11) Ozbay, E. Plasmonics: Merging photonics and electronics at nanoscale dimensions. *Science* **2006**, *311*, 189−193.

(12) Kelly, K. L.; Coronado, E.; Zhao, L. L.; Schatz, G. C. The optical properties of metal nanoparticles: The influence of size, shape, and dielectric environment. *J. Phys. Chem. B* **2003**, *107*, 668−677.

(13) Scholl, J. A.; Koh, A. L.; Dionne, J. A. Quantum plasmon resonances of individual metallic nanoparticles. *Nature* **2012**, *483*, 421−U68.

(14) Link, S.; Wang, Z. L.; El-Sayed, M. A. Alloy formation of gold−silver nanoparticles and the dependence of the plasmon absorption on their composition. *J. Phys. Chem. B* **1999**, *103*, 3529−3533.

(15) Moskovits, M.; Srnova-Sloufova, I.; Vlckova, B. Bimetallic Ag-Au nanoparticles: Extracting meaningful optical constants from the surface-plasmon extinction spectrum. *J. Chem. Phys.* **2002**, *116*, 10435−10446.

(16) Rioux, D.; Vallières, S.; Besner, S.; Muñoz, P.; Mazur, E.; Meunier, M. An analytic model for the dielectric function of Au, Ag, and their alloys. *Adv. Opt. Mater.* **2014**, *2*, 176−182.

(17) Gao, C.; Hu, Y.; Wang, M.; Chi, M.; Yin, Y. Fully alloyed Ag/Au nanospheres: Combining the plasmonic property of Ag with the stability of Au. *J. Am. Chem. Soc.* **2014**, *136*, 7474−7479.

(18) Navas, M. P.; Soni, R. K. Laser generated Ag and Ag−Au composite nanoparticles for refractive index sensor. *Appl. Phys. A: Mater. Sci. Process.* **2014**, *116*, 879−886.

(19) Som, T.; Karmakar, B. Plasmonic AuxAgy bimetallic alloy nanoparticles enhanced photoluminescence upconversion of Er3+ ions in antimony glass hybrid nanocomposites. *J. Mod. Opt.* **2011**, *58*, 1012−1023.

(20) Fan, M. K.; Lai, F. J.; Chou, H. L.; Lu, W. T.; Hwang, B. J.; Brolo, A. G. Surface-enhanced Raman scattering (SERS) from Au:Ag bimetallic nanoparticles: the effect of the molecular probe. *Chem. Sci.* **2013**, *4*, 509−515.

(21) Xu, Q.; Liu, F.; Liu, Y. X.; Cui, K. Y.; Feng, X.; Zhang, W.; Huang, Y. D. Broadband light absorption enhancement in dye-sensitized solar cells with Au-Ag alloy popcorn nanoparticles. *Sci. Rep.* **2013**, *3*, 2112.

(22) Xu, M.; Feng, J.; Liu, Y.-S.; Jin, Y.; Wang, H.-Y.; Sun, H.-B. Effective and tunable light trapping in bulk heterojunction organic solar cells by employing Au-Ag alloy nanoparticles. *Appl. Phys. Lett.* **2014**, *105*, 153303.

(23) Nishi, H.; Torimoto, T.; Tatsuma, T. Wavelength- and efficiency-tunable plasmon-induced charge separation by the use of Au-Ag alloy nanoparticles. *Phys. Chem. Chem. Phys.* **2015**, *17*, 4042−4046.

(24) Xu, Z. C.; Lai, E. C.; Shao-Horn, Y.; Hamad-Schifferli, K. Compositional dependence of the stability of AuCu alloy nano-particles. *Chem. Commun.* **2012**, *48*, 5626−5628.

(25) Chen, H. J.; Shao, L.; Li, Q.; Wang, J. F. Gold nanorods and their plasmonic properties. *Chem. Soc. Rev.* **2013**, *42*, 2679−2724.

(26) Shore, M. S.; Wang, J. W.; Johnston-Peck, A. C.; Oldenburg, A. L.; Tracy, J. B. Synthesis of Au(Core)/Ag(Shell) nanoparticles and their conversion to AuAg alloy nanoparticles. *Small* **2011**, *7*, 230−234.

(27) Fan, J. A.; Wu, C. H.; Bao, K.; Bao, J. M.; Bardhan, R.; Halas, N. J.; Manoharan, V. N.; Nordlander, P.; Shvets, G.; Capasso, F. Self-assembled plasmonic nanoparticle clusters. *Science* **2010**, *328*, 1135−1138.

(28) Sun, Y. G.; Xia, Y. N. Shape-controlled synthesis of gold and silver nanoparticles. *Science* **2002**, *298*, 2176−2179.

(29) Li, C. R.; Lu, N. P.; Mei, J.; Dong, W. J.; Zheng, Y. Y.; Gao, L.; Tsukamoto, K.; Cao, Z. X. Polyhedral to nearly spherical morphology transformation of silver microcrystals grown from vapor phase. *J. Cryst. Growth* **2011**, *314*, 324−330.

(30) Zhou, J.; An, J.; Tang, B.; Xu, S. P.; Cao, Y. X.; Zhao, B.; Xu, W. Q.; Chang, J. J.; Lombardi, J. R. Growth of tetrahedral silver nanocrystals in aqueous solution and their SERS enhancement. *Langmuir* **2008**, *24*, 10407−10413.

(31) Langille, M. R.; Zhang, J.; Personick, M. L.; Li, S. Y.; Mirkin, C. A. Stepwise evolution of spherical seeds into 20-fold twinned icosahedra. *Science* **2012**, *337*, 954−957.

(32) Lee, Y. J.; Schade, N. B.; Sun, L.; Fan, J. A.; Bae, D. R.; Mariscal, M. M.; Lee, G.; Capasso, F.; Sacanna, S.; Manoharan, V. N.; Yi, G. R. Ultrasmooth, highly spherical monocrystalline gold particles for precision plasmonics. *ACS Nano* **2013**, *7*, 11064−11070.

(33) Bosman, M.; Zhang, L.; Duan, H.; Tan, S.; Nijhuis, C. A.; Qiu, C.; Yang, J. K. W. Encapsulated annealing: Enhancing the plasmon quality factor in lithographically−defined nanostructures. *Sci. Rep.* **2014**, *4*, 5537.

(34) Zhang, Q. B.; Xie, J. P.; Liang, J.; Lee, J. Y. Synthesis of monodisperse Ag-Au alloy nanoparticles with independently tunable morphology, composition, size, and surface chemistry and their 3-D superlattices. *Adv. Funct. Mater.* **2009**, *19*, 1387−1398.

(35) Kraus, T.; Malaquin, L.; Schmid, H.; Riess, W.; Spencer, N. D.; Wolf, H. Nanoparticle printing with single-particle resolution. *Nat. Nanotechnol.* **2007**, *2*, 570−576.

(36) Patra, P. P.; Chikkaraddy, R.; Tripathi, R. P. N.; Dasgupta, A.; Kumar, G. V. P. Plasmofluidic single-molecule surface-enhanced Raman scattering from dynamic assembly of plasmonic nanoparticles. *Nat. Commun.* **2014**, *5*, 4357.

(37) Kim, S.; Jung, J. M.; Choi, D. G.; Jung, H. T.; Yang, S. M. Patterned Arrays of Au rings for localized surface plasmon resonance. *Langmuir* **2006**, *22*, 7109−7112.

(38) Maier, S. A.; Brongersma, M. L.; Kik, P. G.; Meltzer, S.; Requicha, A. A. G.; Atwater, H. A. Plasmonics - A route to nanoscale optical devices. *Adv. Mater.* **2001**, *13*, 1501−1505.

(39) Koh, A. L.; Fernandez-Dominguez, A. I.; McComb, D. W.; Maier, S. A.; Yang, J. K. W. High-resolution mapping of electron-beam-excited plasmon modes in lithographically defined gold nanostructures. *Nano Lett.* **2011**, *11*, 1323−1330.

(40) Fowlkes, J. D.; Kondic, L.; Diez, J.; Wu, Y. Y.; Rack, P. D. Self-assembly versus directed assembly of nanoparticles via pulsed laser induced dewetting of patterned metal films. *Nano Lett.* **2011**, *11*, 2478−2485.

(41) Trice, J.; Thomas, D.; Favazza, C.; Sureshkumar, R.; Kalyanaraman, R. Pulsed-laser-induced dewetting in nanoscopic metal films: Theory and experiments. *Phys. Rev. B: Condens. Matter Mater. Phys.* **2007**, *75*, 235439.

(42) Henley, S. J.; Carey, J. D.; Silva, S. R. P. Pulsed-laser-induced nanoscale island formation in thin metal-on-oxide films. *Phys. Rev. B: Condens. Matter Mater. Phys.* **2005**, *72*, 195408.

(43) Fowlkes, J. D.; Wu, Y. Y.; Rack, P. D. Directed assembly of bimetallic nanoparticles by pulsed-laser-induced dewetting: A unique time and length scale regime. *ACS Appl. Mater. Interfaces* **2010**, *2*, 2153−2161.

(44) Wu, Y.; Dong, N.; Fu, S.; Fowlkes, J. D.; Kondic, L.; Vincenti, M. A.; de Ceglia, D.; Rack, P. D. Directed liquid phase assembly of highly ordered metallic nanoparticle arrays. *ACS Appl. Mater. Interfaces* **2014**, *6*, 5835−5843.

(45) McKeown, J. T.; Wu, Y. Y.; Fowlkes, J. D.; Rack, P. D.; Campbell, G. H. Simultaneous in-situ synthesis and characterization of Co@Cu core-shell nanoparticle arrays. *Adv. Mater.* **2015**, *27*, 1060−1065.

(46) Yadavali, S.; Krishna, H.; Kalyanaraman, R. Morphology transitions in bilayer spinodal dewetting systems. *Phys. Rev. B: Condens. Matter Mater. Phys.* **2012**, *85*, 235446.

(47) Herminghaus, S.; Jacobs, K.; Mecke, K.; Bischof, J.; Fery, A.; Ibn-Elhaj, M.; Schlagowski, S. Spinodal dewetting in liquid crystal and liquid metal films. *Science* **1998**, *282*, 916−919.

(48) Li, G. L.; Cherqui, C.; Wu, Y. Y.; Bigelow, N. W.; Simmons, P. D.; Rack, P. D.; Masiello, D. J.; Camden, J. P. Examining substrate-induced plasmon mode splitting and localization in truncated silver nanospheres with electron energy loss spectroscopy. *J. Phys. Chem. Lett.* **2015**, *6*, 2569−2576.

(49) Fowlkes, J. D.; Roberts, N. A.; Wu, Y.; Diez, J. A.; Gonzalez, A. G.; Hartnett, C.; Mahady, K.; Afkhami, S.; Kondic, L.; Rack, P. D. Hierarchical nanoparticle ensembles synthesized by liquid phase directed self-assembly. *Nano Lett.* **2014**, *14*, 774−782.

(50) Kondic, L.; Dong, N.; Wu, Y.; Fowlkes, J. D.; Rack, P. D. Instabilities of nanoscale patterned metal films. *Eur. Phys. J.: Spec. Top.* **2015**, *224*, 369−378.

(51) Tanabe, I.; Tatsuma, T. Plasmonic manipulation of color and morphology of single silver nanospheres. *Nano Lett.* **2012**, *12*, 5418−5421.

(52) Matsubara, K.; Tatsuma, T. Morphological changes and multicolor photochromism of Ag nanoparticles deposited on single-crystalline TiO2 surfaces. *Adv. Mater.* **2007**, *19*, 2802−2806.

(53) Albella, P.; Garcia-Cueto, B.; Gonzalez, F.; Moreno, F.; Wu, P. C.; Kim, T. H.; Brown, A.; Yang, Y.; Everitt, H. O.; Videen, G. Shape matters: plasmonic nanoparticle shape enhances interaction with dielectric substrate. *Nano Lett.* **2011**, *11*, 3531−3537.

(54) Atwater, H. A.; Polman, A. Plasmonics for improved photovoltaic devices. *Nat. Mater.* **2010**, *9*, 205−213.

(55) Li, G. L.; Cherqui, C.; Bigelow, N. W.; Duscher, G.; Straney, P. J.; Millstone, J. E.; Masiello, D. J.; Camden, J. P. Spatially mapping energy transfer from single plasmonic particles to semiconductor substrates via STEM/EELS. *Nano Lett.* **2015**, *15*, 3465−3471.

(56) Bansal, A.; Sekhon, J.; Verma, S. S. Scattering efficiency and LSPR tunability of bimetallic Ag, Au, and Cu nanoparticles. *Plasmonics* **2014**, *9*, 143−150.

(57) Gaudry, M.; Lermé, J.; Cottancin, E.; Pellarin, M.; Vialle, J. L.; Broyer, M.; Prével, B.; Treilleux, M.; Mélinon, P. Optical properties of (AuxAg1-x)(n) clusters embedded in alumina: Evolution with size and stoichiometry. *Phys. Rev. B: Condens. Matter Mater. Phys.* **2001**, *64*, 085407.

(58) Mallin, M. P.; Murphy, C. J. Solution-phase synthesis of sub-10 nm Au-Ag alloy nanoparticles. *Nano Lett.* **2002**, *2*, 1235−1237.

(59) Bigelow, N. W.; Vaschillo, A.; Iberi, V.; Camden, J. P.; Masiello, D. J. Characterization of the electron- and photon-driven plasmonic excitations of metal nanorods. *ACS Nano* **2012**, *6*, 7497−7504.

(60) Peña-Rodríguez, O.; Caro, M.; Rivera, A.; Olivares, J.; Perlado, J. M.; Caro, A. Optical properties of Au-Ag alloys: An ellipsometric study. *Opt. Mater. Express* **2014**, *4*, 403−410.

(61) Schmidt, F.-P.; Ditlbacher, H.; Hohenester, U.; Hohenau, A.; Hofer, F.; Krenn, J. R. Universal dispersion of surface plasmons in flat nanostructures. *Nat. Commun.* **2014**, *5*, 3604.

(62) Cherqui, C.; Thakkar, N.; Li, G.; Camden, J. P.; Masiello, D. J. Characterizing localized surface plasmons using electron energy-loss spectroscopy. *Annu. Rev. Phys. Chem.* **2015**, submitted. doi: 10.1146/annurev-physchem-040214-121612.

(63) Myroshnychenko, V.; Rodríguez-Fern ández, J.; Pastoriza-Santos, I.; Funston, A. M.; Novo, C.; Mulvaney, P.; Liz- Marzán, L. M.; García de Abajo, F. J. Modelling the optical response of gold nanoparticles. *Chem. Soc. Rev.* **2008**, *37*, 1792−1805.

(64) Yamamoto, N.; Ohtani, S.; García de Abajo, F. J. Gap and Mie plasmons in individual silver nanospheres near a silver surface. *Nano Lett.* **2011**, *11*, 91−95.

(65) Liu, Z.; Ji, D.; Zeng, X.; Song, H.; Liu, J.; Jiang, S.; Gan, Q. Surface dispersion engineering of Ag-Au alloy films. *Appl. Phys. Express* **2015**, *8*, 042601.